

# Multidisciplinary Design of S-shaped Intake

J.-M. Zhang<sup>1</sup>, C.-F. Wang<sup>2</sup>, and K.-Y. Lum<sup>3</sup>

*Temasek Laboratories, National University of Singapore,  
10 Kent Ridge Crescent, Singapore 119260, Republic of Singapore*

Because it is multi-objective and multidisciplinary in nature, designing of intake is one of the most demanding tasks. For the first time, this study investigates a design strategy of combining possible multidisciplinary techniques for achieving desirable design of intake with considering both its aerodynamic (AE) and electromagnetic (EM) performances. To facilitate the geometry parameterization of an intake, Hicks-Henne functions are used as basis functions to formulate the variations of centre line, cross-sectional area and aspect ratio. As an attempt, the gappy proper orthogonal decomposition (POD) method is applied for shape optimization to produce optimal solution in a least square sense. Utilizing this strategy, two redesigned S-shaped intakes are proposed based on a baseline duct. The first one tries to improve only the AE performance of baseline intake, while the second one aims at enhancing both its AE and EM performances. The comparisons between these two redesigned intakes indicated that the result of multidisciplinary design is a compromise solution, due to the conflicting requirements from the viewpoints of AE and EM.

## Nomenclature

$DC(\theta)$	= a measure of the flow kinetic energy related to distortion severity, $(P_f - P_\theta)/q_f$
$f(x)$	= parametric function with parameter length $x$ from 0 to 1
$PR$	= duct pressure recovery, $P_f/P_{f,in}$
$P_f$	= mean total pressure at the engine face
$P_{f,in}$	= mean total pressure at the inlet face
$P_\theta$	= minimum average total pressure over a sector of angle $\theta$ at the engine face
$q_f$	= mean dynamic pressure at the engine face
$SC(\theta)$	= a measure of the severity of the secondary flows, $(V_{CF\_MAX} - V_{CF\_MIN})/V_{AVE}$
$P^i$	= design parameters for the $i$ -th snapshot
$R^i$	= SCS solutions for the $i$ -th snapshot
$S^i$	= flow solutions for the $i$ -th snapshot
$U(x, t)$	= flow field solution
$V_{AVE}$	= average axial flow velocity
$V_{CF\_MAX}$	= maximum average secondary flow over a sector of angle $\theta$ at the engine face
$V_{CF\_MIN}$	= minimum average secondary flow over a sector of angle $\theta$ at the engine face
$V^i$	= augmented $i$ -th snapshot for POD analysis
$z$	= lateral coordinate (on the plane of symmetry)
$\alpha_i, b_i$	= coefficient of the $i$ -th mode in a function expansion
$\beta_j^i$	= $j^{\text{th}}$ element of the $i^{\text{th}}$ eigenvector
$\lambda^i$	= eigenvalues from $i^{\text{th}}$ eigenvector
$\Phi^i$	= $i$ -th POD basis vector
$  \cdot  $	= $L^2$ -norm

<sup>1</sup> Research Scientist, Temasek Laboratories, National University of Singapore, 10 Kent Ridge Crescent, Singapore 119260

<sup>2</sup> Senior Research Scientist, Temasek Laboratories, National University of Singapore, 10 Kent Ridge Crescent, Singapore 119260

<sup>3</sup> Principal Research Scientist, Temasek Laboratories, National University of Singapore, 10 Kent Ridge Crescent, Singapore 119260

## I. Introduction

Intake design is one of the most demanding tasks of developing the aircraft propulsion system, as it is multi-objective and multidisciplinary in nature. The solution is generally a compromise between a number of conflicting goals<sup>1</sup>. One of these conflicts is due to the different requirements from the viewpoints of aerodynamics (AE) and electromagnetics (EM). In terms of aerodynamics, the role of the intake is to provide the engine with sufficient mass flow at optimum levels of total pressure and flow uniformity, which are vital for engine operability and stability. Thus highly curved intake must be avoided as the bent shape yields cross-stream pressure gradients, which in turn produce secondary flows along the walls leading to flow separation and nonuniform velocity<sup>2</sup>. On the other hand, to prevent the intake from being detected by EM sensors, it is essential to minimize the electromagnetic (EM) scattering cross section (SCS) of the intake shape by offsetting the engine from the intake face, to the extent that the rotating fan blades are shielded from any EM sensors<sup>3</sup>. This usually leads to the highly convoluted intake ducts, which are notorious for flow distortion and flow swirl<sup>3</sup>. As a first attempt, this study aims at finding a compromise solution of the intake shape design, which will enhance both AE and EM performances of the baseline duct.

In respect of shape optimization, some research works have been carried out in the field of aerodynamics, by coupling a computational fluid dynamics (CFD) software with an optimization algorithm. The optimization algorithms applied to intake design focus on the use of gradient-based optimization techniques<sup>4-9</sup> and stochastic optimization methods<sup>10-11</sup>. The former require modifying the flow solver to calculate additional gradients, hence adding complexity and have the potential of being trapped into a local minimum, while the latter need large computation cost for function evaluations. Due to the difficulty of incorporating the electromagnetic calculations into the CFD simulation, and the large computational cost of both CFD and EM simulations, there is a great demand for finding a new methodology to the multidisciplinary design of intakes.

As proper orthogonal decomposition (POD) has the capability to obtain low-dimensional approximate descriptions of a high-dimensional process<sup>12</sup>, it will be beneficial in reducing computational cost. In addition to being optimal in a least square sense, POD representation is completely data dependent and does not assume any prior knowledge on how the data are initially generated. These advantages promote the applications of POD technique in wide-ranging fields, such as derivation of reduced-order dynamical model<sup>14</sup>, image processing<sup>15</sup> and pattern recognition<sup>16</sup>. The method of “snapshots” and “gappy POD” introduced by Sirovich<sup>17</sup> and Everson and Sirovich<sup>18</sup> further impel the applications of POD technique into the numerical simulations of fluid flows, such as studies reported by Bui-Thanh et al.<sup>19</sup>, Venturi and Karniadakis<sup>20</sup>, Willcox<sup>21</sup> and Gunes et al.<sup>22</sup>. The purpose of the present research is to extend the gappy POD approach to the multidisciplinary design of intakes, which is inspired by the previous successful work of applying gappy POD to improve the AE performance of intakes<sup>23</sup>.

In this paper, the gappy POD approach is firstly outlined, followed by a description of the duct parameterization, numerical simulations (in the respects of AE and EM respectively) and the design strategy. Preliminary studies of intake shape optimization, concerning only AE performance on the one hand, and considering both AE and EM performances on the other hand, are presented to demonstrate how the gappy POD method can be used for intake design. Finally, some conclusions are made.

## II. Theory and Methodology

### A. Gappy Proper Orthogonal Decomposition (POD)

The usage of gappy POD in this study is to reconstruct a vector of  $\mathbf{g}$ , having some missing (shape parameters) and known (target properties of intake) elements, so that the reconstructed vector  $\tilde{\mathbf{g}}$  provides the shape parameters, which lead to the desirable properties of intake in the sense of least square optimal. To realize this reconstruction, the basis vectors ( $\Phi$ ) are firstly extracted from the given snapshots  $V$ , which include the information of both shape parameters and the corresponding intake’s properties. Then the reconstructed vector  $\tilde{\mathbf{g}}$  can be represented by  $\tilde{\mathbf{g}} \approx \sum_{i=1}^p b_i \Phi^i$ . Here the coefficients  $b_i$  are such that they minimize the error  $\varepsilon$  between the original and repaired vectors,  $\varepsilon = \|\mathbf{g} - \tilde{\mathbf{g}}\|_a^2$ . Detailed information of the basic and gappy POD theories can be found in Ref.<sup>17-22</sup>. Here only brief procedures are summarized as follows<sup>17-22</sup>.

1) Construct the correlation matrix  $R$  by computing the inner product between every pair of snapshots as shown in Eq. (1).

$$R_{ik} = \frac{1}{m} (\mathbf{V}^i, \mathbf{V}^k) \quad (1)$$

2) Solve the eigen-problems of Eq. (2) to get the eigen vectors of  $\beta_j^i$

$$R\beta = \beta\Lambda \quad (2)$$

3) Get the POD basis vector  $\Phi^i$ , by Eq. (3)

$$\Phi^i = \sum_{j=1}^m \beta_j^i V^j \quad (3)$$

4) Define a “mask” vector, which describes where the information of  $g$  is missing. The corresponding mask vector  $n^k$  can be defined as follows:

$$n^k = 0 \text{ if } g^k \text{ is missing; } n^k = 1 \text{ if } g^k \text{ is known}$$

5) Construct matrix  $M$  and vector  $f$  by using gappy inner product, formulated as  $(u, v)_n = ((n, u), (n, v))$ .

$$M_{ij} = (\Phi^i, \Phi^j)_n \text{ and } f_i = (g, \Phi^i)_n \quad (4)$$

6) Select the number of modes ( $p$ ) to be employed in the reconstruction, by considering the relative “energy” (measured by the 2-norm) captured by the  $i^{th}$  basis vector  $(\lambda^i / \sum_{i=1}^m \lambda^i)$  and condition number of matrix  $M$ .

7) Solve the linear system  $Mb = f$  to get the coefficients  $b_i$ .

8) Reconstruct a new vector as  $\tilde{g} \approx \sum_{i=1}^p b_i \Phi^i$  and replace the missing elements in  $g$  by the corresponding repaired elements in  $\tilde{g}$ , i.e.  $g_i = \tilde{g}_i$  if  $n^i = 0$ .

## B. Parameterization of Duct Geometry

In short, parameterization of duct geometry is the process of defining the parameters to represent the shape of intake. The conventional geometric representation methods based on superposition, such as Hicks-Henne functions, Chebyshev polynomials, etc., are widely used in transonic wing-section design because it conserves the smoothness of airfoil line<sup>24</sup>. Recently, Non-Uniform Rational B-Spline (NURBS) equations are applied as a new shape function to secure a sufficient design space in case the geometric changes are severe<sup>8</sup>. However, NURBS needs more computational cost and has the tendency to produce wavy solutions due to the usage of a large number of control points as design variables. To balance the computational cost and design space, Hicks-Henne functions are used as basis functions in this study as they have proven to be quite effective in realizing design improvements with a limited number of design variables<sup>25</sup>.

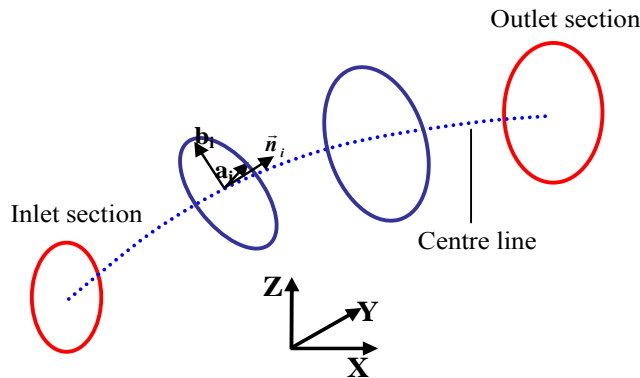


Figure 1. Schematic representation of intake.

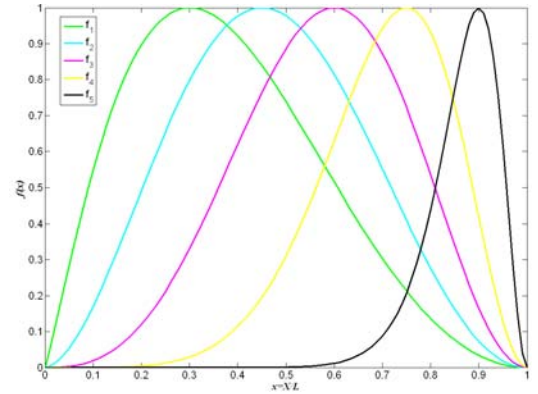


Figure 2. Plots of the used Hicks-Henne functions.

Here, the intake surface is treated as a series of the cross sections, varied along the centre line as shown in Fig. 1. As a preliminary study, each cross-section is assumed to be elliptical, oriented along the normal of center line ( $\vec{n}$ ) and symmetrical about the  $x$ - $z$  plane. If the basic centerline coordinate is represented by  $z_{basic}(x)$ , the parameterized  $z$  coordinate can be expressed as Eq. (5).

$$z(x) = z_{basic}(x) + \sum_{k=1}^N \alpha_k f_k(x) \quad (5)$$

Here Hicks-Henne functions having five members are used as basis functions. They have the format as following:

$$f_k(x) = \sin^2(\pi x^{e(k)}) \quad (6)$$

where  $e(k) = \log(0.5)/\log(x_k)$ ,  $x_k = 0.30, 0.45, 0.60, 0.75, 0.9$  for  $k = 1, 2, 3, 4, 5$ .

The plots of these basis functions are shown in Fig. 2. It can be observed that each basis function has its own main contribution in a particular region of x-coordinate. It is worth noting that the intake length ( $L$ ) in the x-coordinate is fixed and used to obtain the parameter length ( $x=X/L$ ), which varies from 0 to 1.

Prior to the parameterization study, these five basis functions have been tested to be able to represent the intake centre line with comparatively smooth variations. Once defining the centre line, the cross-section planes can be located as they are perpendicular to the centerline. From the inlet to the outlet, the cross-sectional area may be varied. This variation can be expressed as Eq. (7).

$$S(x) = S_{\text{basic}}(x) + \sum_{k=N+1}^{2N} \alpha_k f_{k-N}(x) \quad (7)$$

where  $S_{\text{basic}}(x)$  represents the area variations for the baseline model. Thus the cross-sectional area can be represented as  $A(x) = A_1 + (A_2 - A_1) * S(x)$ , where  $A_1$ ,  $A_2$  represent the throat and engine area respectively. The equivalent radius of each cross-section ( $r(x)$ ) is then equal to  $\sqrt{A(x)}$ . The long and short axes of each ellipse can be separately obtained by Eqs. (8) and (9).

$$a(x) = r(x) * K(x) \quad (8)$$

$$b(x) = r(x) / K(x) \quad (9)$$

The scaling factor  $K$  is also represented by the Hicks-Henne functions,

$$K(x) = K_{\text{basic}}(x) + \sum_{k=2N+1}^{3N} \alpha_k f_{k-2N}(x) \quad (10)$$

Therefore, the problem of defining intake shape can be solved once  $z(x)$ ,  $S(x)$ ,  $a(x)$  and  $b(x)$  are known, which can be obtained by Eqs.(5-10). As the contribution of each basis function is determined by the coefficients (design variables)  $\alpha_k$  of that function, the total number of design parameters is  $3N$  ( $=15$ ). Among them, the first 5 determine the variations of centerline, while the second and last 5 delineate the variations of cross-sectional area and aspect ratio.

Once these design parameters and the related information for the baseline intake are known, a MATLAB program is used to automatically generate the corresponding duct surface. Figs. 3(a), (b) and (c) show the plots of the centerline, area and aspect ratio variations for the baseline model. It is worth noting that the centerline is scaled-down based on the length  $L$  (0.160504m) in the  $x$  coordinate. The area of inlet ( $A_1$ ) and outlet ( $A_2$ ) is equal to  $1.809 \times 10^{-3} \text{ m}^2$  and  $2.533 \times 10^{-3} \text{ m}^2$ .

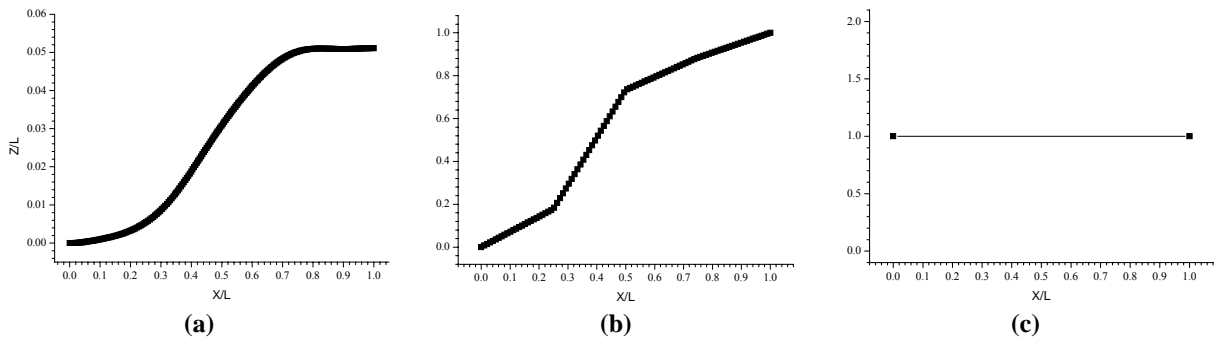


**Figure 3. Plots of (a) centre line (b) cross-sectional and (c) aspect ratio variations for baseline model.**

Figures 4 (a) and (b) show the plots of cross-section lines and surface of this baseline intake created in MATLAB. It is worth noting that these cross-section lines are perpendicular to the centerline. The information of surface points is written as the Plot3D format, so as to be imported into GAMBIT to further build the three-dimensional (3D) geometry and meshes for CFD calculation as shown in Fig. 4 (c). As the S-shaped duct is assumed to be symmetric, only half of the models are built. To focus on the flow characteristics along the centerline, the 3D structured meshes are parallel to the z-coordinate, instead of being perpendicular to the centerline. At the same time, the geometry information is exported as \*.stp file to facilitate the later SCS calculation. The same techniques are used to create a set of snapshots (intakes). To be time efficient, GAMBIT journal files are specified to build the

geometry, meshes and export the files into the commercial software of Patran and Fluent respectively. These journal files can be executed in batch mode.

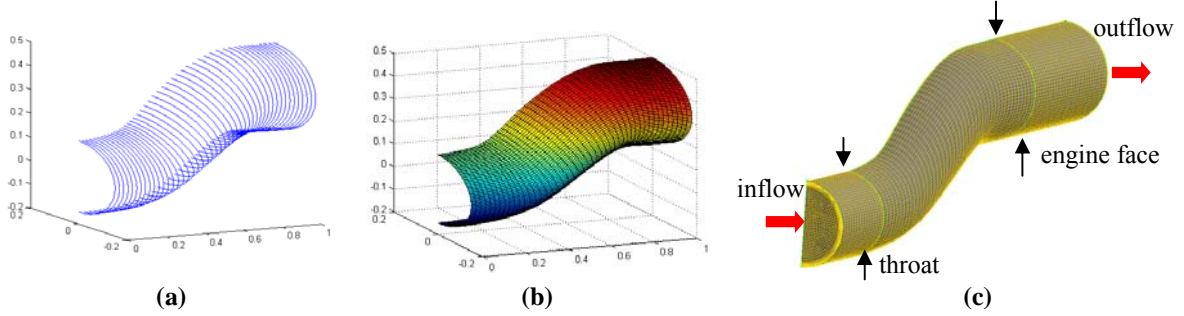


**Figure 4. Plots of (a) cross-section lines (b) surface and (c) volume meshes created for baseline intake.**

### C. CFD Simulation

In order to allow for specification of unidirectional inflow condition, the computational inflow boundary is placed at a distance ( $D_1=0.048\text{m}$ ) upstream of the throat as shown in the Fig. 4 (c). The inflow is assumed to be  $15.4\text{m/s}$  of velocity and has the properties of  $\rho=1.2\text{kg/m}^3$  and  $\mu=1.8\times 10^{-5}\text{Pa}\cdot\text{s}$ . Static pressure is specified at the outflow boundary, which is placed sufficiently downstream of the engine face (at  $1.75D_1$ ) to prevent this uniform cross-stream pressure specification from affecting the natural development of the flow within the S-duct. The structured meshes contain 192,556 cells. Grids are clustered near the wall, so as to fulfill the condition of  $y^+\approx 1$  and allow appropriate resolution of the boundary layer.

The commercial software FLUENT is adopted in this study to calculate the flow in the duct, and the governing equations are the Reynolds averaged Navier-Stokes (RANS) equations. As the Reynolds stresses are included in the momentum conservation equations, to complete these equations, a turbulent model is required to predict the Reynolds stresses with sufficient accuracy. Preceding researchers have proposed that two-equation turbulence models predict the duct flow better than the algebraic and one-equation models<sup>26</sup>. Therefore the Shear-Stress Transport (SST)  $k-\omega$  model is applied here due to its ability to take into account the turbulent boundary layer history effect by solving the complete transport equations of  $k$  and  $\omega$ . To be time efficient, FLUENT journal files are specified to set up the boundary conditions, required convergence levels and the turbulence model etc. These journal files can be executed in batch mode.

In order to characterize the flow of intake, several indicators are available to judge the intake aerodynamic performance<sup>27</sup>. The  $DC(\theta)$  parameter examines the flow distortion based upon total pressure values in sectors of angle  $\theta$  at the engine face. This parameter can be roughly interpreted as a measure of the flow distortion severity. It is quantified as:

$$DC(\theta) = \frac{P_f - P_\theta}{q_f} \quad (11)$$

where  $P_f$  is the mean total pressure at engine face,  $P_\theta$  is the minimum average total pressure over a sector of angle  $\theta$  at the engine face, and  $q_f$  is the corresponding mean dynamic pressure. The sector must be significant extinct and a commonly used coefficient is  $DC(60)$ .

The flow can also be characterized by examining the magnitude of the secondary flow or swirl velocities<sup>28</sup>. The  $SC(\theta)$  parameter provides a measure of the severity of the flow swirling that may lead to a stalling of the compressor blades:

$$SC(\theta) = \frac{V_{CF\_MAX} - V_{CF\_MIN}}{V_{AVE}} \quad (12)$$

where  $V_{CF\_MAX}$  and  $V_{CF\_MIN}$  represent the maximum and minimum average secondary flow over a sector of angle  $\theta$  at engine face separately and  $V_{AVE}$  represents the average axial flow velocity at engine face. In this study,  $SC(60)$  is used to judge the magnitude of flow swirl.

Another typical flow descriptor is the intake pressure recovery<sup>28</sup>. This parameter characterizes the efficiency of the diffuser to convert kinetic energy to pressure energy:

$$PR = \frac{P_f}{P_{f\_in}} \quad (13)$$

where  $P_{f,in}$  is the mean total pressure at throat face. As these descriptors work together to assess the aerodynamic performances of intakes, a program in C is written as a User Defined Function (UDF) of FLUENT to automatically obtain these predictors at the end of iterations.

#### D. SCS Simulation

Efficient modeling of electromagnetic scattering from intake or cavity structure is one of the most important and challenging topics in the research area of computational electromagnetics. As reviewed in<sup>29</sup>, many studies have been carried out for the analysis of the electromagnetic scattering from cavity structures for years. Several typical methods have been proposed to handle various cavity structures from different points of view and all the methods developed have different features. The study along this direction can help us to accurately characterize the effects of the cavity on the overall electromagnetic scattering response of real target. This has motivated the development of accurate and efficient methods to model the electromagnetic scattering of cavity structure.

The finite element-boundary integral (FE-BI) method is an effective and fast method to model EM scattering from open cavities, which can be arbitrarily-shaped and inhomogeneously-filled<sup>30</sup>. However, for a cavity that is large and deep, there are two important issues to be considered in the FE-BI method: reduction in computational complexity, and numerical dispersion error. Recently, the combination of FE-BI method and a higher-order algorithm has been proposed to effectively reduce the numerical dispersion error for the analysis of large and deep cavity<sup>30-35</sup>. The higher-order algorithm includes two aspects: (1) higher-order geometrical modeling, by which the shape of cavity can be more accurately modeled; (2) higher-order field modeling, by which the dispersion error can be reduced and convergence of the solution is improved. On the other hand, the choice of a proper solver is critical to the efficient determination of the solution. The conjugate gradient method and fast Fourier transformation (CG-FFT), an iterative method, can be used as a solver for the FE-BI method. However, as the number of unknowns increases, the convergence of the CG-FFT solver deteriorates, or may not be reached. In contrast, the frontal method, which is a direct method, is a feasible approach to analyze backscattering from a deep cavity using the FE-BI technique. The use of the frontal method in the FE-BI also reduces the computational complexity in the solution of large and deep cavity problem.

Through using the frontal solver, higher-order FE-BI method can efficiently handle the electromagnetic scattering from large and deep cavities. Temasek Laboratories @ NUS has successfully developed an in-house higher-order FE-BI code, namely *FEBI-HOE*, which has been extensively validated and verified through the comparison of numerical and experimental results. The detailed description of the method used for the in-house *FEBI-HOE* code can be found from<sup>34-35</sup>. In this study, the in-house code *FEBI-HOE* is used as a tool to calculate the SCS of interior scattering from intakes.

#### E. Duct Design Strategy

The schematic chart for the optimal design of intake is presented in Fig. 5.

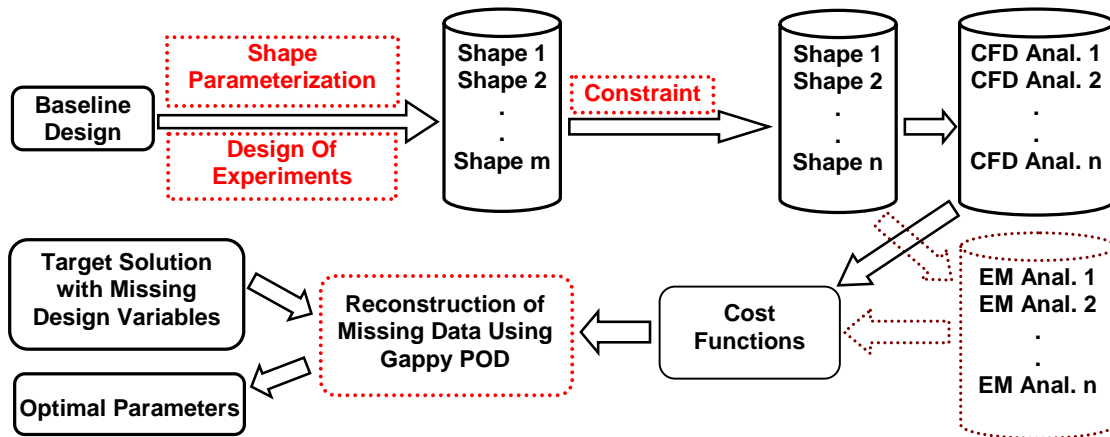


Figure 5. Schematic chart for optimal design of S-shaped intake.

As per the duct parameterization, an intake can be generated once the information on design parameters and baseline model (with respect to the centerline, cross-sectional area and aspect ratio variations) are known. To create

a set of snapshots, Design of Experiments (DOE) can be used to generate the corresponding design parameters as this approach will ensure that the snapshots better span the design space. In this study, the Bose orthogonal array proposed by Owen<sup>36</sup> is used for generating this set of orthogonal design parameters, within the variation ranges of all design parameters. Here, each of these 15 design parameters is assumed to be varied with 32 levels within the specified variation range, as shown in the third and fourth columns of Table 1.

**Table 1. Summary of design parameters to describe the intake**

Parameters		Min	Max	Values for redesigned intake (AE)	Values for redesigned intake (AEEM)
Central line	$\alpha_1$	-0.02	0.02	-1.3543455e-002	-7.2909553e-003
	$\alpha_2$	-0.2	0.2	1.0863856e-001	3.9668960e-002
	$\alpha_3$	-0.2	0.2	-7.4626483e-002	-3.9744004e-002
	$\alpha_4$	-0.02	0.02	-1.7791696e-002	-7.9167186e-003
	$\alpha_5$	-0.01	0.01	4.6430911e-003	4.0932328e-004
Area Size Variations	$\alpha_6$	-0.1	0.1	8.4540194e-002	6.9658024e-002
	$\alpha_7$	-0.1	0.1	3.5967140e-002	-2.3978160e-002
	$\alpha_8$	-0.3	0.3	-9.4328805e-003	-3.1667395e-002
	$\alpha_9$	-0.2	0.2	-1.0932680e-001	-1.4012120e-001
	$\alpha_{10}$	-0.06	0.06	-7.0553454e-002	-1.4076841e-003
Aspect Ratio Variations	$\alpha_{11}$	0	0.01	1.9146471e-003	6.4806450e-003
	$\alpha_{12}$	0	0.06	4.5015318e-002	1.6903535e-002
	$\alpha_{13}$	0	0.01	9.1695185e-003	7.5630000e-003
	$\alpha_{14}$	0	0.1	1.9629063e-002	2.1516789e-003
	$\alpha_{15}$	0	0.02	-7.0769177e-003	4.0142447e-003

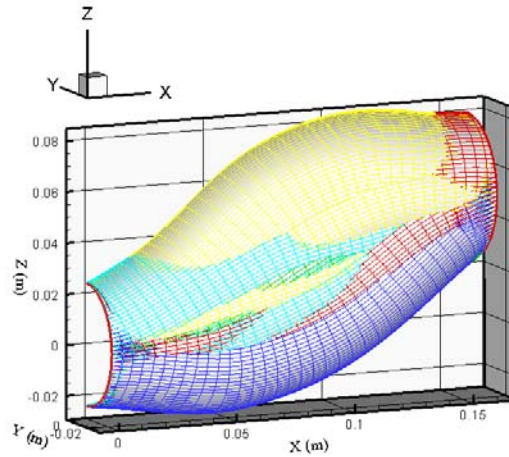


**Figure 6. Surfaces of the half S-ducts for the snapshots generated with constraint.**

So the corresponding Bose orthogonal array is a matrix of 1024 ( $32^2$  as it has strength of 2) rows and 15 columns. That means the total number of experiments is 1024. As some combinations of design parameters cannot satisfy  $0 \leq S(x) \leq 1$ , only 612 geometries can be created based on the available combinations of design parameters. However, it will be very time consuming to fully investigate all these 612 intakes. To reduce the computational cost of CFD and SCS simulations, a constraint on the local wall angle is enforced to select only 22 geometries from all these intakes for further simulation. The local wall angle is defined as the maximum variation of tangential angles (with respect to the  $x$ -axis) at two adjoining points along the upper and lower walls. This methodology was used by Ghate et al.<sup>37</sup> for local fidelity analysis. The idea is derived from industry practices whereby the geometry



parameters of average diffusion angle, radius of mean flow line, equivalent duct radius and local wall angle can be used for quick design of ducts that are free from undesirable phenomenon, like flow separation and rapid boundary layer growth, due to excessive diffusion rates or acute bends, both locally and globally. In this study, the local wall angle of snapshots is limited to be less than 9 degree. The surfaces of the half S-ducts for these selected 22 snapshots are shown in Fig. 6.

The CFD and SCS solutions are then carried out for each snapshot separately. Extracting important flow and SCS solutions for this set of snapshots can construct a dataset together with the corresponding design parameters. For example, this set of data can be built as  $V^i = [P^i \ S^i \ R^i]^T$ , where  $P^i$  represents the design parameters;  $S^i$  and  $R^i$  represent the total pressure distributions at the engine face and SCS characteristics for the  $i^{th}$  snapshot, respectively. Therefore, given a target of total pressure distributions at the engine face and SCS characteristics, the target vector  $V^* = [P^* \ S^* \ R^*]^T$  can then be considered as an incomplete data vector, where the total pressure ( $S^*$ ) and SCS information ( $R^*$ ) are known, whereas the design parameters ( $P^*$ ) remain to be determined. Utilizing the gappy POD procedures outlined in the Section II (A), the values of the design parameters ( $P^*$ ) can be determined. Based on the design parameters obtained, a redesigned duct can be created.

Besides the multidisciplinary design to achieve a redesigned duct, which has better both AE and EM performances, another gappy POD study based on pure aerodynamic performance is also carried out. The procedure is the same as that delineated in the previous paragraph, except that the SCS solutions will be ignored. The following section reports the results based on these two case studies.

### III. Results and Discussion

As described earlier, two gappy POD investigations have been carried out to redesign the same baseline intake, so as to achieve better AE performance on the one hand, and improve both AE and EM performances on the other hand. Detailed results will be delineated in this Section. It is worth noting that convergence tests are carried out for the dataset according to the method proposed by Bendat and Piersol<sup>38</sup> before the gappy POD investigations. These tests are to examine the convergence of statistics in a mean square sense, so as to ensure that enough data is available for the newly created dataset. The successful convergence tests are obtained for all the data analyzed confirm that the created dataset is sufficient to represent the statistical characteristics of the flow and SCS.

#### A. Optimal Design to Improve Only AE Performance

In this section, an example of optimal design for S-duct is presented as Case 1. The design objective is to obtain a new intake that has better AE performance than that of the baseline one. The target model is a straight duct, which has the same throat and engine faces as the baseline duct. Assumption of straightness (the vertical distance between the throat and engine faces is zero) guarantees uniform flow to the engine with optimal total pressure as shown in Figs. 7 (a) and (b) separately.

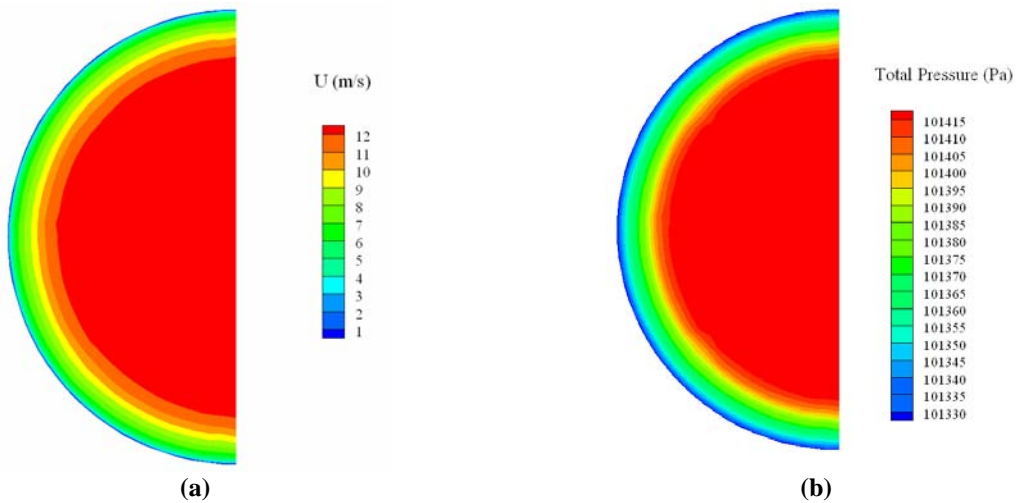


**Figure 7. (a) Axial velocity and (b) total pressure distributions at the engine face of the target straight duct.**



Figures 8 (a) and (b) show the comparisons of total pressure and non-axial momentum distributions at the engine face of the baseline and redesigned models. To facilitate the comparison, the left half of each figure represents the results of the baseline model, while the right half demonstrates the results of redesigned model. Lower total pressure can be observed from Fig. 8 (a) at the top and bottom parts of the baseline model. This is due to the turning of duct curvature. In contrast with the baseline model, the low total-pressure region has been eliminated from the bottom part of the redesigned duct, whereas at the top part of the engine face the low-total-pressure region is smaller in size, as observed in Fig. 8 (a). The comparison of non-axial momentum distributions at the engine face in Fig. 8 (b) demonstrates that the redesigned duct has less non-axial momentum, viz. less flow swirl than the baseline one, especially at the top part of the engine face. A small flow-swirl region near the bottom part of the baseline intake is also eliminated in the redesigned duct. At the same time, the maximum non-axial momentum is reduced greatly from  $17.8 \text{ m}^2/\text{s}^2$  (for the baseline model) to  $6.0 \text{ m}^2/\text{s}^2$  (for the redesigned duct). All these results indicate that the redesigned intake has been improved over the baseline model in terms of weakening the flow swirl and flow distortion.

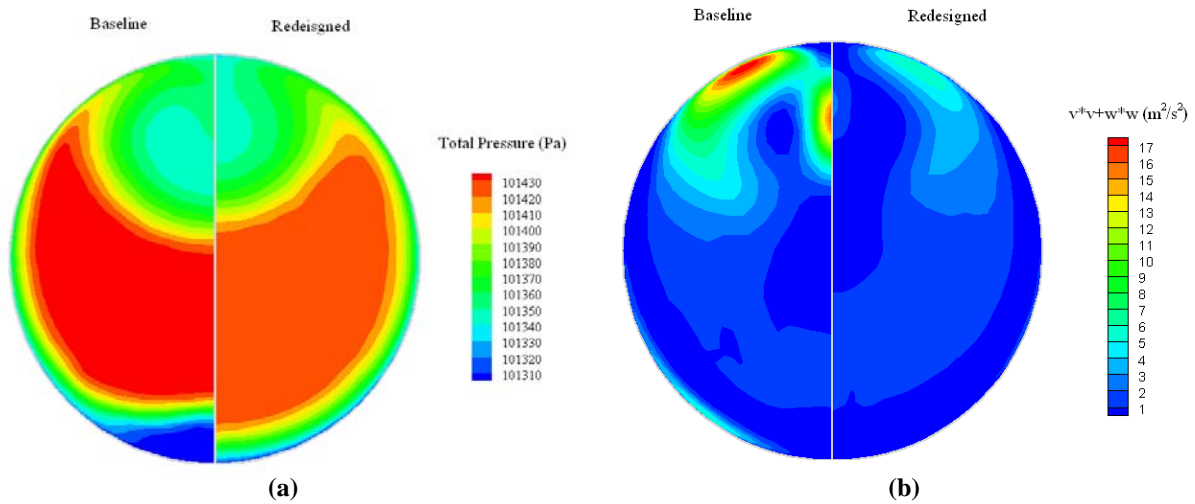


**Figure 8. Comparisons of (a) total pressure and (b) non-axial momentum distributions at the engine face of baseline and redesigned ducts from Case 1 (to improve only AE performance).**

To further compare the baseline and redesigned models, Figs. 9 (a) and (b) show the velocity vectors and axial velocity distributions at the symmetry planes of these two models, respectively. From Fig. 9 (a), it can be observed that the baseline model has two flow recirculation regions. One is near the top wall; the other is near the bottom wall. Within these regions, the flow direction changes due to the large pressure gradient, which results in total pressure loss. Unlike the baseline model, the redesigned duct has only one recirculation region near the top wall and this recirculation region is smaller in size than that of the baseline one, which can be easily observed in Fig. 9 (b) as the negative axial velocity is represented in white color. This reduction of recirculation region in both number and size for the redesigned duct is advantageous for achieving a uniform flow at the engine face.

As summarized by Herry<sup>39</sup>, pressure loss in the flow of duct is mainly due to flow separation. He suggested that the forces arising in the airstream in a direction opposite to the direction of flow together with the change of flow direction in bends, tended to cause flow separation. As it can be seen, the curvature changes of the redesigned model conform better to the flow path than that of the baseline model. Therefore, in the redesigned model, flow separation and overall elbow pressure loss as well as the secondary flow are weakened.

To quantitatively assess the aerodynamic performance of the redesigned duct, Table 2 tabulates the values of AE performance indicators such as PR, DC(60) and SC(60) for the baseline and redesigned models. As the assumption of incompressible fluid is made due to the low inlet velocity, the variations of total pressure loss are small as seen in Table 2. But it can be found that the redesigned model for Case 1 has less total pressure loss (18.1 Pa) than that of the baseline one (31.1 Pa), which implies that the redesigned intake can provide more mass flow rate than that of the baseline model if they are working under the same pressure condition. In addition, the redesigned duct for Case 1 shows improvement in AE performance, which is achieved by reducing the flow distortion and flow swirl and improving the duct pressure recovery as indicated by the lower values of DC(60) and SC(60), and the higher values

of PR than those of the baseline model. The values for the straight duct are also tabulated for reference, but which are impossible to be exactly reached by the redesigned model due to the constraint of the vertical distances between the throat and engine faces. Discussions for the EM performances of these intakes will be delineated in the next section.

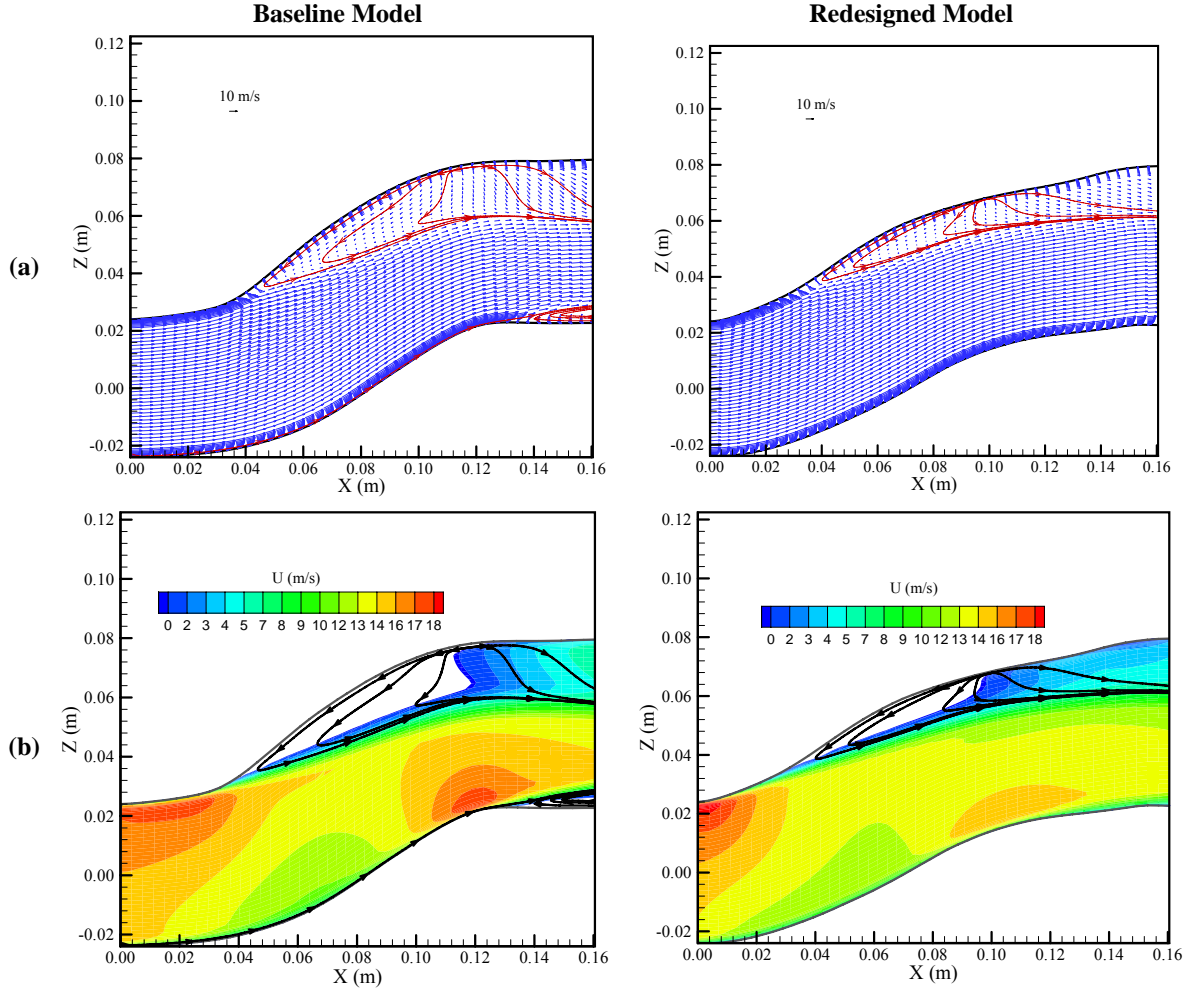


Figure 9 (a) Velocity vectors and (b) axial velocity distributions at the symmetry plane of baseline and redesigned ducts from Case 1 (to improve only AE performance).

Table 2. Comparisons of AE performance indicators for baseline and 2 redesigned models

	Baseline Model	Redesigned Models		Straight Intake
		Case 1 (AE)	Case 2 (AEEM)	
Total Pressure Loss (Pa)	31.1	<b>18.1</b>	<b>19.3</b>	10.1
PR	0.999693	<b>0.999821</b>	<b>0.999809</b>	0.999900
DC(60)	0.546048	<b>0.528377</b>	<b>0.543641</b>	0.009156
SC(60)	0.194942	<b>0.119808</b>	<b>0.136808</b>	0.007212

## B. Multidisciplinary Design To Improve Both AE and EM Performances

In this section, an example of multidisciplinary design of the S-duct by taking into account both AE and EM performances is presented as Case 2. The design objective is to obtain a new intake that has better performance, both aerodynamically and electromagnetically, than those of the baseline. The target values of the CFD solutions is the same as that of previous investigation, viz. the target model is a straight duct, which has the same throat and engine

faces as those of the baseline duct. But the choice of target values for EM solutions is debatable. The EM performance of a straight intake is usually worst in most situations. To minimize the SCS of the intake shape, it is necessary to offset the engine from the intake face to the extent that the rotating fan blades are shielded from any EM system<sup>1</sup>. So the objective of this study is confined to providing a new design, whose EM performance is better than that of the straight duct. Although the SCS characteristics for S-shaped intakes are wavy as a function of the angle of incidence, **the target SCS values are finally chosen to be the value of the maximum SCS of the straight duct minus 10 dBsm in magnitude for all the angles investigated.**

In order to assess the AE performance of redesigned duct (for Case 2), Figs. 10 (a) and (b) show the comparisons of the total pressure and non-axial momentum distributions of the baseline and redesigned models at the engine face. From Fig. 10 (a), it can be observed the low-total-pressure region at the bottom part of the baseline model has been eliminated from the redesigned duct. The latter also has a smaller low-total-pressure region in size than that of the baseline one, at the top part of engine face as observed in Fig. 10 (a). The comparison of non-axial momentum distributions at engine faces in Fig. 10 (b) demonstrates that the redesigned duct has less non-axial momentum, viz. less flow swirl than that of the baseline one, especially at the top part of engine face. The maximum non-axial momentum is reduced from  $17.8\text{m}^2/\text{s}^2$  (of baseline model) to  $9.3\text{m}^2/\text{s}^2$  (for the redesigned duct). This indicates that, the redesigned intake is better than the baseline model in terms of weakening the flow swirl and flow distortion. However, it can be seen that the AE performance of this redesigned duct is worse than that of the redesigned one obtained from Case 1 (which concerns only AE performance) as the maximum non-axial momentum can be reduced to  $6.0\text{m}^2/\text{s}^2$  in that case.

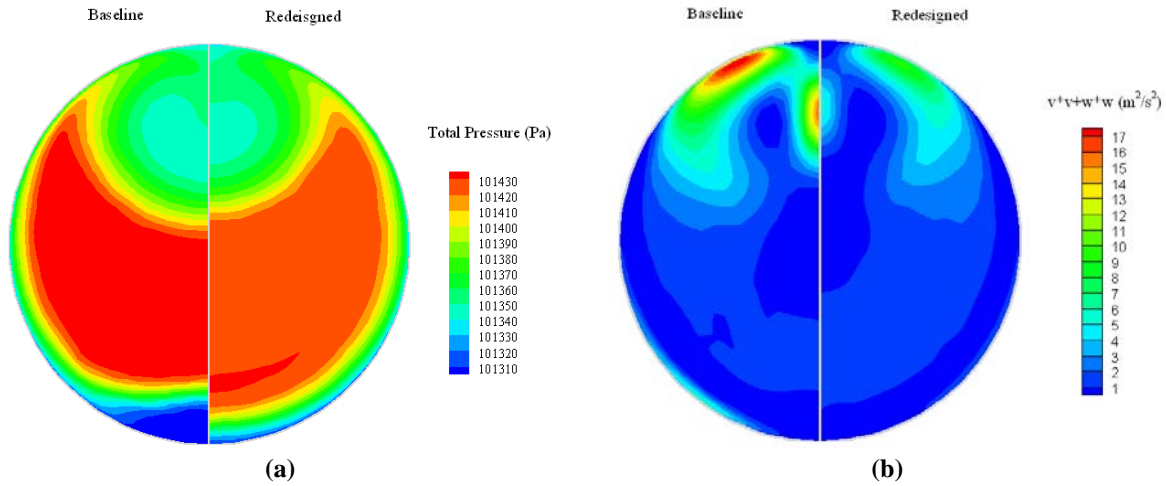


**Figure 10. Comparisons of (a) total pressure and (b) non-axial momentum distributions at the engine face of baseline and redesigned ducts for Case 2 (to improve both AE and EM performances).**

To further compare the baseline and redesigned intakes, Figs. 11 (a) and (b) show the velocity vectors and axial velocity distributions at the symmetry plane for these two models. From Fig. 11 (a), it can be observed that the redesigned duct has only one recirculation region near the top wall, and this recirculation region is smaller in size than that of the baseline one. The reduction of the recirculation region in both number and size implies that flow separation and overall elbow pressure loss as well as the secondary flow are weakened in the redesigned model. These are advantageous for achieving a uniform flow at the engine face.

To quantitatively evaluate the AE performance of the redesigned duct, we can refer to Table 2. As in Case 1, the redesigned model for Case 2 has less total-pressure loss than that of the baseline one, which implies its ability to provide more mass flow rate for the engine than the baseline model if they work under the same pressure condition. In addition, the redesigned duct shows improvement in AE performance, which is indicated by the lower values of DC(60), SC(60) and the higher values of PR than those of the baseline model. However, the redesigned duct for multidisciplinary study (Case 2) has worse AE performance than that of the optimal design concerning only AE performance (Case 1) as indicated by the lower PR and higher DC(60), SC (60) and total pressure loss values, than those of the redesigned model obtained from Case 1. That is to say that some advantages of AE performance are lost for the redesigned model, so as to achieve improvement in EM performance.

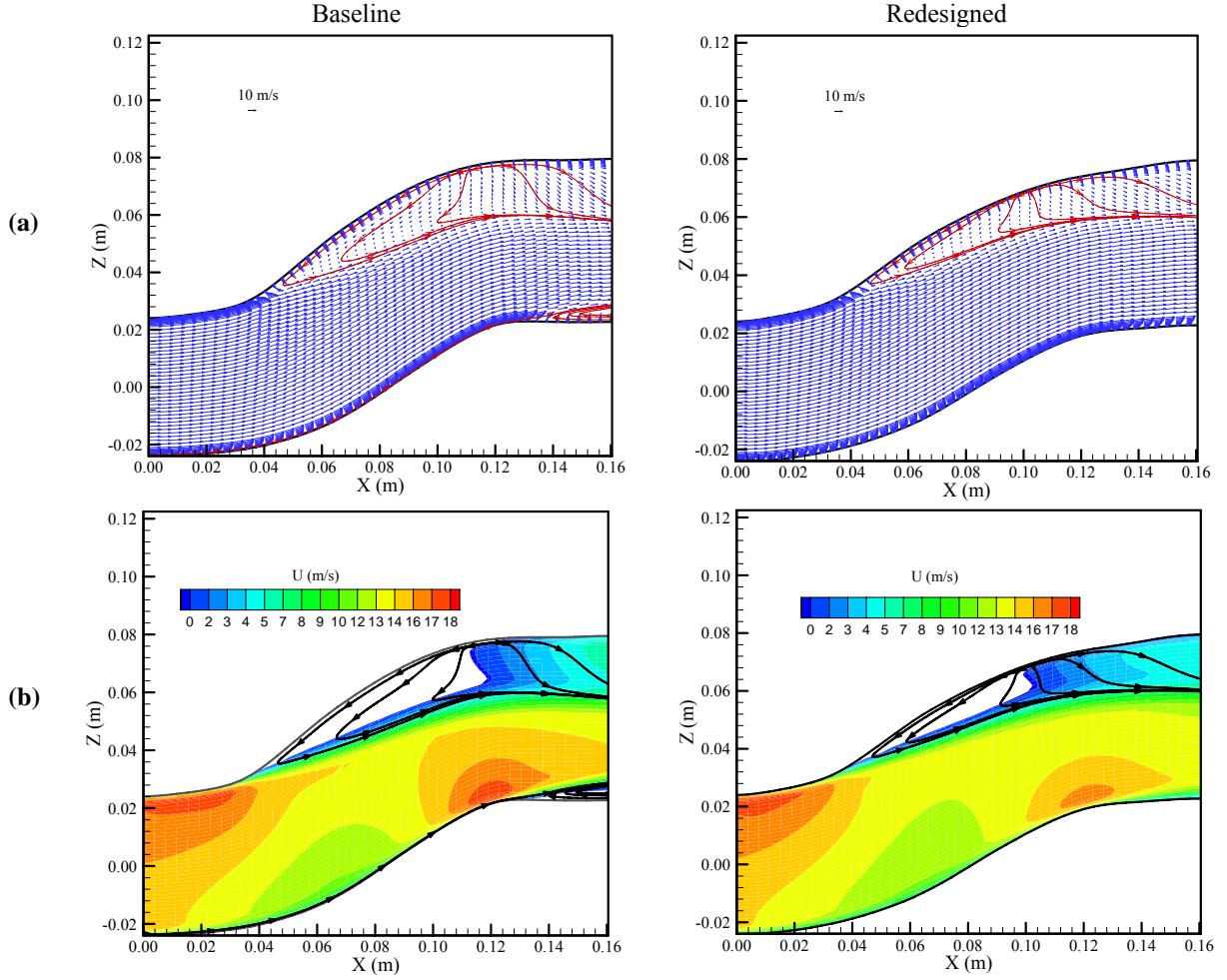


**Figure 11. (a) Velocity vectors and (b) axial velocity distributions at the symmetry plane of baseline and redesigned ducts for Case 2 (to improve both AE and EM performances).**

To compare the EM performances of all these intakes, the operating frequency is fixed at 10 GHz for all the SCS calculations. Fig. 12 shows the SCS values of the straight duct, baseline duct, and redesigned ducts from Case 1 and Case 2 studies. It is worth noting that the figure in the middle of Fig. 12 shows the coordinate system used for EM investigations, which is different from that of CFD simulation. The following descriptions of planes are related to the coordinate system shown in the Fig. 12. As it can be seen from Fig. 12(a), the straight duct has the highest maximum monostatic SCS of -13.34 dBsm at  $\theta=0^\circ$  for the  $\theta\theta$ -polarization in the  $xz$ -plane. Compared with the straight duct, the baseline model has lower maximum monostatic SCS of -15.13 dBsm at  $\theta=6.5^\circ$  due to its curvature in the  $xz$ -plane. By virtue of the same mechanism, both two redesigned models have even lower maximum SCS values (-17.03dB and -21.34dB) than that of the baseline one, and the corresponding angles for these maximum values are shifted further to be at  $\theta=17.5^\circ$  and  $34^\circ$ , respectively. For the  $\phi\phi$ -polarization in the  $xz$ -plane; the same phenomena can be found as shown in Fig. 12 (b). The maximum SCS value of -13.34dBsm at  $\theta=0^\circ$  for the  $\phi\phi$ -polarization of the straight intake is reduced to -14.49dBsm at  $\theta=7^\circ$  for the baseline model. By virtue of the geometry changes in the  $xz$ -plane, the redesigned models from Case 1 and Case 2 have maximum values of -15.79dBsm at  $\theta=-23.5^\circ$  and -17.53dBsm at  $\theta=-25^\circ$ , respectively.

In the  $yz$ -plane, it can be observed that the straight duct still has maximum SCS values of -13.34dB at  $\theta=0^\circ$  for both the  $\theta\theta$ - and  $\phi\phi$ -polarizations due to its symmetry. All of the models have maximum SCS values for the  $\theta\theta$ -polarization at  $\theta=0^\circ$  as illustrated in Fig. 12 (c). The baseline model has a maximum SCS value of -16.03 dBsm that is lower than that of the straight one for  $\theta\theta$ -polarization. Both redesigned models have lower maximum SCS values (-19.16dBsm and -20.77dBsm, respectively) than that of the baseline one. Unlike in the previous finding, for the  $\theta\theta$ -

polarization, the redesigned model from Case 1 has a slightly lower peak value than that of the redesigned model from Case 2. This is because the  $\theta\theta$ -polarizations in the  $yz$ -plane at  $\theta=0^\circ$  shall be the same as those of  $\phi\phi$ -polarizations in the  $xz$ -plane at  $\theta=0^\circ$ . Similarly, Fig. 12 (d) shows the  $\phi\phi$ -polarization values for all the models. The maximum  $\phi\phi$ -polarization value for the baseline duct is -15.63 dBsm at  $\theta=0^\circ$ , which is lower than that of the straight intake. Also both of the redesigned ducts have smaller peak values than that of the baseline one. Although the maximum  $\phi\phi$ -polarization values of -18.89dBsm of redesigned model from Case 2 is larger than that of the redesigned model from Case 1 (-20.45dBsm), its corresponding incidence angle is shifted to  $\pm 20.5^\circ$  instead of  $0^\circ$ .

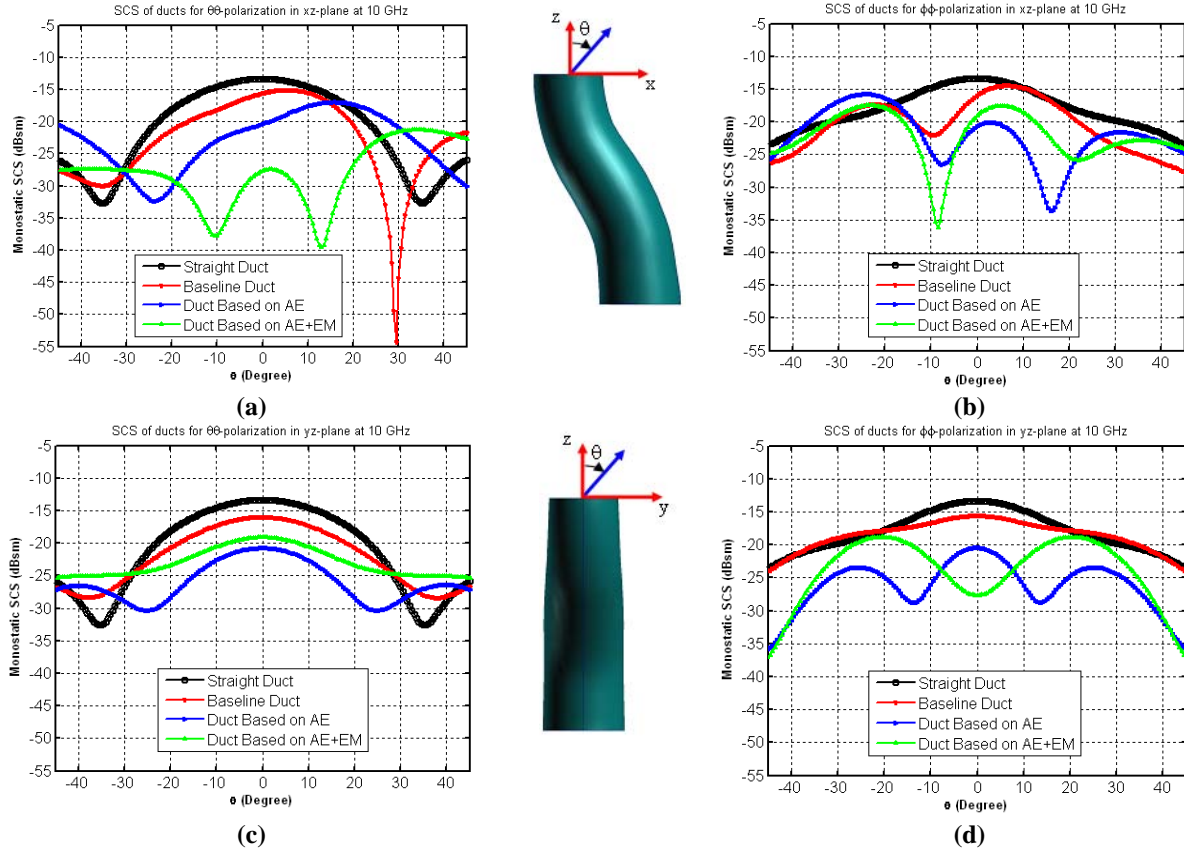


**Figure 12. Comparisons of EM performance for baseline, straight and redesigned ducts from Case 1 (to improve only AE performance) and Case 2 (to improve both AE and EM performances) studies.**

In general, both two redesigned models have better EM performances than that of the baseline one. In addition, the redesigned duct from Case 2 has a better EM performance than that of the redesigned model from Case 1 in terms of both the  $\theta\theta$ - and  $\phi\phi$ -polarizations in the  $xz$ -plane. Although the results for the polarizations at  $yz$ -plane yield adverse results, it can be understood as the current investigation only focuses on the bending in the  $xz$ -plane without changing the cross sectional shape of the duct. Also, for smaller incidence angles ( $-15^\circ$  to  $15^\circ$ ), the redesigned duct from Case 2 can be observed to have lower peak polarization values than those of the redesigned intake from Case 1, except for the  $\phi\phi$ -polarization in the  $yz$ -plane as shown in Fig. 13.

It can be said that better improvement in EM performance, for the  $\theta\theta$ -polarization in the  $xz$ -plane, has been achieved in the redesigned duct of Case 2 than that of Case 1, as seen in Fig. 13 (a). Meanwhile, the improvements for  $\theta\theta$ -polarization in the  $yz$ -plane, as well as the  $\phi\phi$ -polarizations in both planes, are not distinct or very slight. This is due to the fact that bending of the centre line in the  $xz$ -plane mainly only affects the  $\theta\theta$ -polarization in the  $xz$ -plane. To further improve the overall EM performance, bending the centre line in both the  $xz$ - and  $yz$ -planes is necessary as discussed in Ref. 40.

In summary, both redesigned ducts have better AE and EM performances than those of the baseline one. However the redesigned duct obtained from the multidisciplinary design has worse AE and better EM performances



(especially for  $\theta\theta$ -polarization in  $xz$ -plane) than those of the redesigned intake obtained by considering only AE performance. This is due to the conflicting requirements from the viewpoints of AE and EM performances. To achieve the improvement of EM performance, some advantages in AE performance are sacrificed. The final result is a compromise between these two conflicting goals.

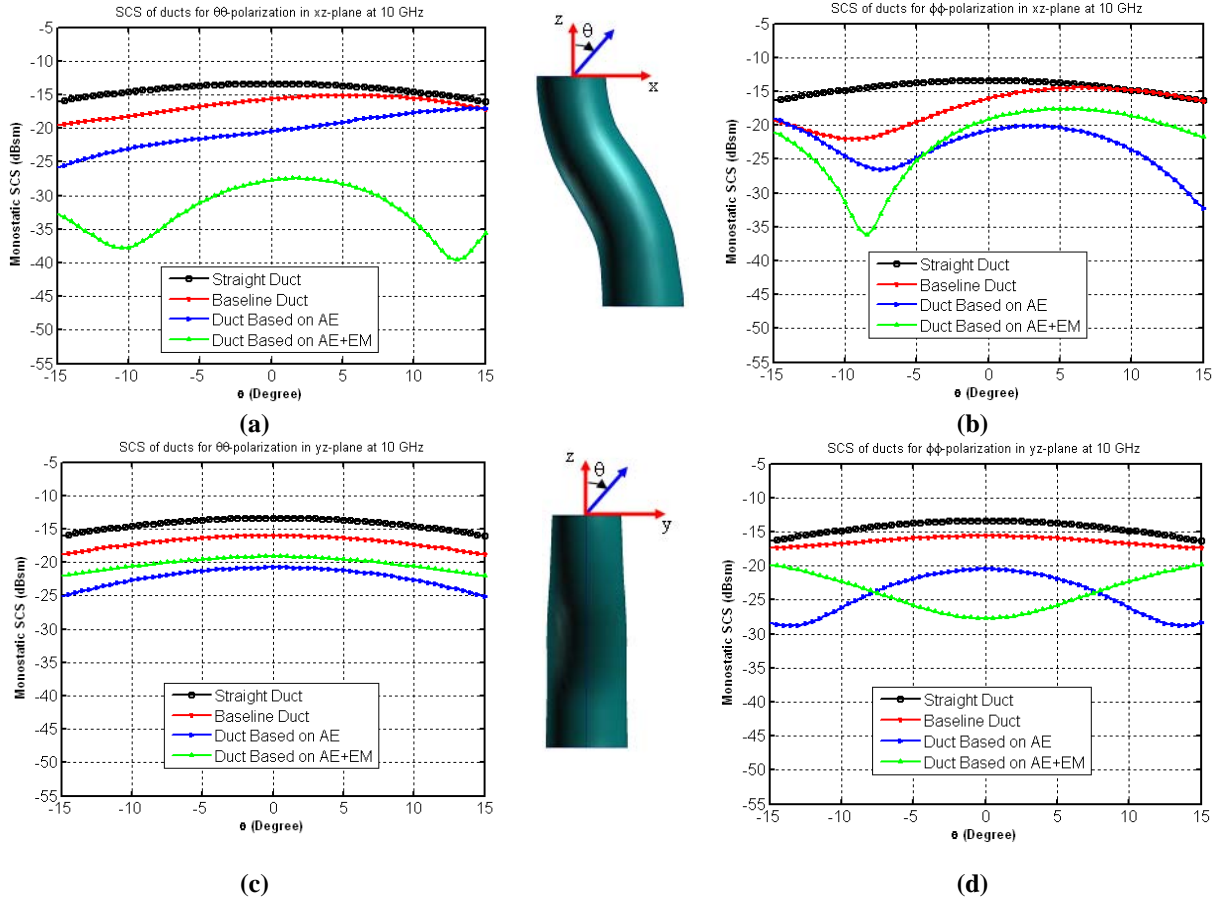


Figure 13. Zoom-in of Figure 12.

#### IV. Conclusion

In brief, this study investigates intake design from the viewpoint of both AE and EM performances. To facilitate the design, Hicks-Henne functions have been used for intake shape parameterization. As shown in Table 1, an intake can be easily generated once the design parameters are decided for a given baseline model.

Two examples of intake design using gappy POD methodology are presented. The first one aims at improving only AE performance, while the second one tries to improve both AE and EM performances. Both redesigned ducts have better AE and EM performances than that of the baseline one. However the redesigned duct obtained from the multidisciplinary design has worse AE but better EM performances (essentially, the  $\theta\theta$ -polarization in the  $xz$ -plane) than that of the redesigned intake obtained by considering only AE performance. This is due to the conflicting requirements of AE and EM for intake shape design. To balance these conflicting goals, some advantages in AE performance is traded off for improving EM performance in the multidisciplinary study.

Using the gappy POD methodology, many (15) design variables can be obtained at the same time, which is more efficient than other methods, such as the gradient optimisation of Sayed and Berry<sup>41</sup>. They took 8h CPU time to optimize a single design variable and 72.5h for taking four variables into consideration. As it only takes a few minutes to compute the POD modes and finish subsequent gappy POD calculation, the computational cost of this study is mainly for the AE and EM simulations of snapshots. In this respect, adding the constraint of local wall angle for creating snapshots is valuable, as fewer simulations are required to provide optimal design. As reported in this paper, based on the information obtained with only 22 snapshots, the strategy utilizing gappy POD investigation is

able to greatly improve the duct performance in the present study, which is more efficient than the method of Gaiddon et al.<sup>11</sup>, who evaluated a total of 3271 designs to optimise the duct.

It should be emphasized, however, that the POD redesign approach consists in linear interpolation of the snapshots to arrive at the closest match, in the linear least-squares sense, of the target performances. Whereas the physical problem is highly nonlinear, such as AE and EM, the actually achievable performances may be significantly different. This is also evident in the present studies, where the final AE and EM performances are not exactly same as their targets. In addition, the construction of the snapshot dataset is crucial for the achievable results. Therefore, exploitation of domain knowledge and engineering know-how in snapshot creation will greatly enhance the effectiveness of POD redesign.

Finally, although this methodology has provided promising results for intake design, further investigation to consider the centreline variations in both  $xz$ - and  $yz$ -planes and the cross-sectional shape variations are necessary for multidisciplinary study, so as to achieve the improvement of EM performance for both  $\theta\theta$ - and  $\phi\phi$ -polarizations in both  $xz$ - and  $yz$ -planes. Compressible flow characteristics and SCS at higher frequency range shall also be investigated before utilizing this methodology in industrial design.

### Acknowledgments

The authors would like to thank Professor Hock Lim for his invaluable comments and advices. The authors would also like to thank Mr. Shyam Sundar Dhanabalan for sharing his knowledge on geometry generation. J.-M. Zhang and C.-F. Wang would like to thank Dr. Her Mann Tsai for initiating the LO inlet and exhaust research program.

### References

- <sup>1</sup>Sóbeseter, A., "Tradeoffs in Jet Inlet Design: a Historical Perspective," *Journal of Aircraft*, Vol. 44, No. 3, 2007, pp.705-717.
- <sup>2</sup>Mayer, D. W., Anderson, B. H., and Johnson, T. A., "3D Subsonic Diffuser Design and Analysis," *34<sup>th</sup> AIAA/ASME/SAE/ASEE Joint Propulsion Conference and Exhibit*, AIAA 98-3418, 1998.
- <sup>3</sup>Thordson, L., "Combat Survivability with Advanced Aircraft Propulsion Development," *Journal of Aircraft*, Vol. 19, No. 11, 1982, pp.915-920.
- <sup>4</sup>Wu, X., Cliff, E. M., and Gunzburger, M.D., "An Optimal Design Problem for a Two-dimensional Flow in a Duct," *Optim. Contr. Appl. Met.*, Vol. 17, 1996, pp. 329-339.
- <sup>5</sup>Herdman, T. L. A., "Structured Reduced Sequential Quadratic Programming and its Application to a Shape Design Problem," *Comput. Optim. Appl.*, Vol. 11, 1998, pp.81-100.
- <sup>6</sup>Zhang, W., Knight, D., and Smith, D., "Automated Design of a Three Dimensional Subsonic Diffuser," *J. Propul. Power*, Vol.16, No. 6, 2000, pp. 1132-1140.
- <sup>7</sup>Taskinoglu, E., and Knight, D., "Multi-objective Shape Optimization Study for a Subsonic Submerged Inlet," *J. Propul. Power*, Vol. 20, No. 4, 2004, pp. 620-633.
- <sup>8</sup>Lee, B. J., Kim, C., and Rho, O.H., "Optimal Shape Design of the S-shaped Subsonic Intake Using NURBS," *43<sup>th</sup> AIAA Aerospace Science Meeting and Exhibit*, AIAA-2005-455, 2005.
- <sup>9</sup>Zhang, Z., and Lum, K., "S-Shaped Inlet Design Optimization Using the Adjoint Equation Method," *42<sup>nd</sup> AIAA/ASME/SAE/ASEE Joint Propulsion Conference and Exhibit*, Sacramento, AIAA-2006-4453, 2006.
- <sup>10</sup>Zha, G. C., Smith, D., Schwabacher, M., Rasheed, K., Gelsey, A., Knight, D., and Haas, M., "High Performance Supersonic Missile Inlet Design Using Automated Optimization," *J Aircraft*, Vol. 34, No. 6, 1997, pp. 697-705.
- <sup>11</sup>Gaiddon, A., Knight, D. D., and Poloni, C., "Multicriteria Design Optimization of a Supersonic Inlet Based Upon Global Missile Performance," *J. Propul. Power*, Vol. 20, No. 3, 2004, pp. 542-558.
- <sup>12</sup>Chatterjee, A., "An Introduction to the Proper Orthogonal Decomposition," *Current Science*, Vol. 78, No. 7, 2000, pp. 808-817.
- <sup>13</sup>Rathinam, M., and Petzold, L. R., "A New Look at Proper Orthogonal Decomposition," *SIAM J. Numer. Anal.*, Vol. 41, No. 5, 2003, pp. 1893-1925.
- <sup>14</sup>Holmes, P., Lumley, J., and Berkooz, G., *Turbulence, Coherent Structures, Dynamical Systems and Symmetry*, Cambridge University Press, Cambridge, UK, 1996.
- <sup>15</sup>Sirovich, L., and Kirby, M., "Low-dimensional Procedure for the Characterization of Human Faces," *J. Opt. Soc. Am A.*, Vol. 4, No. 3, 1987, pp. 519-524.
- <sup>16</sup>Fukunaga, K., *Introduction to statistical pattern recognition*, New York, Academic Press, 1972.
- <sup>17</sup>Sirovich, L., "Turbulence and Dynamics of Coherent Structures. Part 1: Coherent Structures," *Q. Appl. Math.*, Vol. 45, No. 3, 1987, pp. 561-571.
- <sup>18</sup>Everson, R., and Sirovich, L., "The Karhunen-Loève Procedure for Gappy Data," *J. Opt. Soc. Am.*, Vol. 12, 1995, pp. 1657-1664.
- <sup>19</sup>Bui-Thanh, T., Damodaran, M., and Willcox, K., "Aerodynamic Data Reconstruction and Inverse Design Using Proper Orthogonal Decomposition," *AIAA Journal*, Vol. 42, No. 8, 2004, pp. 1505-1516.



- <sup>20</sup>Venturi, D., and Karniadakis, G., "Gappy Data and Reconstruction Procedures for Flow Past a Cylinder," *J. Fluid Mech.*, Vol. 519, 2004, pp. 315-336.
- <sup>21</sup>Willcox, K., "Unsteady Flow Sensing and Estimation via the Gappy Proper Orthogonal Decomposition," *Computers & Fluids*, Vol. 35, 2006, pp. 208-226.
- <sup>22</sup>Gunes, H., Sirisup S., and Karniadakis, G. E., "Gappy Data: to Krig or not to Krig?" *Journal of Computational Physics*, Vol. 212, 2006, pp. 358-382.
- <sup>23</sup>Zhang, J.-M., Dhanabalan, S. S. and Tsai, H. M., "Optimal design of intake using gappy POD," *TL-AE-07-02*, 2007.
- <sup>24</sup>Zhang, Z., and Lum, K., "Airfoil Optimization Design of Drag Minimization with Lift Constraint Using Adjoint Equation Method," *44th AIAA Aerospace Sciences Meeting and Exhibit*, AIAA-2006-55, 2006.
- <sup>25</sup>Reuther, J., Jameson, A., Farmer, J., Martinelli, L., and Saunders, D., "Aerodynamic Shape Optimization of Complex Aircraft via an Adjoint Formulation," *34th AIAA Aerospace Science Meeting and Exhibit*, AIAA-96-0094, 1996.
- <sup>26</sup>Yaras, M. I., and Grosvenor, A. D., "Evaluation of One- and Two-equation Low-Re Turbulence Models. Part II-Vortex-Generator Jet and Diffusing S-duct Flows," *Int. J. Numer. Meth. Fluids*, Vol. 42, 2003, pp. 1321-1343.
- <sup>27</sup>Seddon, J., and Goldsmith, E. L., *Intake Aerodynamics: an Account of the Mechanics of Flow in and Around the Air Intakes of Turbine-Engined and Ramjet Aircraft and Missiles*, London, Collins Professional and Technical Books, 1985.
- <sup>28</sup>Harrison, N. A., Anderson, J., Fleming, J. L., and Ng, W. F., "Computer Analysis of Active Flow Control of a Boundary Layer Ingesting Serpentine Inlet Diffuser," *44th AIAA Aerospace Sciences Meeting and Exhibit*, AIAA-2006-874, Reno, Nevada, 2006.
- <sup>29</sup>Anastassiou, H. T., "A Review of Electromagnetic Scattering Analysis for Inlets, Cavities, and Open Ducts," *IEEE Antennas Propagat. Mag.*, Vol. 45, No. 6, pp. 27-40.
- <sup>30</sup>Jin, J. M., "Electromagnetic Scattering from Large, Deep, and Arbitrarily-Shaped Open Cavities," *Electromagn.*, Vol. 18, 1998, pp. 3-34.
- <sup>31</sup>Graglia, R. D., Wilton, D. R., and Peterson, A. F., "Higher Order Interpolatory Vector Bases for Computational Electromagnetics," *IEEE Trans. Antennas Propagat.*, Vol. 45, 1997, pp. 329-342.
- <sup>32</sup>Jin, J. M., Liu, J., Lou, Z., and Liang, C. S. T., "A Fully Higher-Order Finite-Element Simulation of Scattering by Deep Cavities," *IEEE Trans. Antennas Propagat.*, Vol. 51, 2003, pp. 2420-2429.
- <sup>33</sup>Liu, J., and Jin, J. M., "A Special Higher Order Finite-Element Method for Scattering by Deep Cavities," *IEEE Trans. Antennas Propagat.*, Vol. 48, 2000, pp. 694-703.
- <sup>34</sup>Hu, F. G., Wang, C. F., Gan, Y. B., and Xu, Y., "Modeling of Interior Scattering from 3D Cavity Using FE-BI Method with Higher-Order Tetrahedral Element," *IEEE APS Int. Symp.*, Vol. 1, 2005, 105-108.
- <sup>35</sup>Hu, F. G., Wang, C. F., and Gan, Y. B., "Efficient Calculation of Interior Scattering from Large Three-Dimensional PEC Cavities," *IEEE Trans. Antennas Propagat.*, Vol. 55, No. 1, 2007, pp. 167-177.
- <sup>36</sup>Owen, A. B., "Orthogonal Arrays for Computer Experiments, Integration and Visualization," *Statistica Sinica*, Vol. 2, 1992, pp. 439-452.
- <sup>37</sup>Ghate, D., Isaacs, A., Sudhakar, K., Mujumdar, P. M., and Marathe, A.G., "3d-Duct Design Using Variable Fidelity Method," *10th AIAA/ISSMD Multi-disciplinary Analysis and Optimization*, AIAA-2004-4427, New York, 2004.
- <sup>38</sup>Bendat, J., and Piersol, A., *Random Data: Analysis and Measurement Procedures*, 3rd edn., Wiley, New York, 2000.
- <sup>39</sup>Herry, J. R., "Design of Power-Plant Installations Pressure-Loss Characteristics of Duct Components," *NACA Wartime Rept. WC-93*, 1943.
- <sup>40</sup>Wang, C. F., Hu, F. G., and Gan, Y. B., "Numerical Modeling of the Effect of Cavity Wall Profile on Interior Scattering from Large PEC Cavity," *IEEE APS Int. Symp.*, 2007, pp. 2498-2501.
- <sup>41</sup>Sayed, M. E., Sun, T., and Bettry, J., "Shape Optimisation with Computational Fluid Dynamics," *Adv. Eng. Softw.*, Vol. 36, 2005, pp. 607-613.